EES Solar

PAPER

View Article Online
View Journal | View Issue

Cite this: *EES Sol.*, 2025, **1**, 182

Synergistic solar-powered water–electricity cogeneration using a 3D-printed heatsink-like device†

Na Li,‡[ab] Jintao He,‡[ab] Jingjing Li,[a] Zhaojun Li,[c] Petri Murto,[de] Zhihang Wang *[fg] and Xiaofeng Xu *[a]

Received 24th December 2024
Accepted 26th February 2025

DOI: 10.1039/d4el00041b

rsc.li/EESSolar

The application of solar energy for both power generation and water production is widely regarded as a promising solution for addressing global shortages in electricity and water resources. Solar-driven interfacial evaporation, with its controllable thermal conversion process, has emerged as an ideal platform for simultaneously producing water and energy. Herein, we present an efficient hybrid system for freshwater and thermoelectricity generation, featuring a thermoelectric generator (TEG) embedded in a heatsink-like monolithic nanocellulose aerogel steam generator (SG) constructed *via* 3D printing. The strategy of cold evaporation cooling (CEC) optimizes the use of waste heat from hybrid modules and environmental energy, while simultaneously minimizing heat conduction losses. This is achieved by improving the energy exchange between the photothermal evaporation module and the thermoelectric generation module, as well as between the cold evaporation surface and the surrounding environment. Consequently, the CEC-induced hybrid system obtains a maximum power density of 0.19 W m^{-2} and an outstanding water evaporation rate of 2.65 kg m^{-2} h^{-1} under 1 sun (AM 1.5G) illumination, which are 365% and 203% higher than those of devices without the CEC effect. The synergistic enhancement of solar-driven evaporation and thermoelectricity sheds light on the development of more efficient and customized solar thermal applications.

Broader context

Solar-driven water–energy cogeneration has garnered significant attention as a promising solution to water scarcity and electricity shortages. However, the lack of synergy of conventional devices and inefficient integration limit the practical use and extensive deployment of solar-driven water–electricity cogeneration. Here, we introduce a novel hybrid device design strategy for a 3D freshwater–thermoelectricity generator that integrates a thermoelectric generator (TEG) with a monolithic steam generator (SG). The device features a heatsink-like configuration, where the photothermal conversion layer serves as the hot end of the TEG, and the cold evaporation surface functions as the cold end, thereby maximizing the utilization of both solar and environmental energy. This innovative structural design enhances the cold evaporation cooling effect, efficiently dissipates heat at the cold end, and enables long-term, stable electricity generation. Additionally, the cold evaporation surface boosts the intake of ambient energy, further increasing the water evaporation rate. As a result, the hybrid system achieves synergistic enhancement of water–electricity cogeneration, simultaneously attaining high evaporation rates and stable thermoelectric electricity generation. This work paves the way for further research into high-performance water–electricity cogeneration and expands its potential for application-specific innovations.

1. Introduction

Global challenges such as freshwater scarcity and electricity shortages are intensifying due to factors like rapid population growth, urbanization, overuse of water resources, and the impacts of climate change.[1–3] Desalination technology is a critical approach to mitigating the shortage of freshwater resources, holding particular significance for arid regions and

[a]*College of Materials Science and Engineering, Ocean University of China, Qingdao, 266404, China. E-mail: xuxiaofeng@ouc.edu.cn*

[b]*School of Rehabilitation Sciences and Engineering, University of Health and Rehabilitation Sciences, Qingdao, 266113, China*

[c]*Solid State Physics Division, Department of Materials Science and Engineering, Uppsala University, Lägerhyddsvägen 1, Uppsala, 751 03, Sweden*

[d]*Yusuf Hamied Department of Chemistry, University of Cambridge, Cambridge, CB2 1EW, UK*

[e]*Department of Chemistry and Materials Science, Aalto University, Kemistintie 1, Espoo, 02150, Finland*

[f]*School of Engineering, College of Science and Engineering, University of Derby, Markeaton Street, Derby DE22 3AW, UK. E-mail: z.wang@derby.ac.uk*

[g]*Department of Materials Science and Metallurgy, University of Cambridge, 27 Charles Babbage Road, Cambridge, CB3 0FS, UK*

† Electronic supplementary information (ESI) available. See DOI: https://doi.org/10.1039/d4el00041b

‡ These authors contributed equally to this work.

island nations.[4–6] However, traditional seawater desalination methods, such as reverse osmosis, multi-stage flash distillation, and multi-effect evaporation, are highly energy-intensive and demand significant electricity and fossil fuel consumption, further aggravating energy crises and environmental pollution. Consequently, significant efforts have been devoted to investigating the energy–water nexus.[7–11] Solar energy, being one of the Earth's most abundant energy sources, offers numerous advantages, including safety, cleanliness, renewability, sustainability, low cost, and ease of accessibility, making it a highly promising alternative energy source.[12–15] Given these advantages, solar-driven interfacial evaporation, an efficient, low-carbon, and sustainable water purification technology, is extensively applied in wastewater treatment,[16–19] desalination,[20–24] directional salt crystallization,[25–29] and water–energy cogeneration,[30–33] playing a crucial role in alleviating freshwater shortages.

Given the current energy crisis and freshwater scarcity, solar-driven water–electricity cogeneration emerges as a promising technology for both freshwater production and green power generation.[34–37] In recent years, various solar-driven water–electricity cogeneration systems based on the hydrovoltaic effect,[38–41] photovoltaic effect,[42] salinity gradient effect,[43–45] piezoelectric effect,[46,47] and temperature gradient effect[48–50] have been developed. The performance of hydrovoltaic and salinity gradient systems is typically constrained by the availability of advanced generator materials (electrical conductivity, specific surface area, wettability, *etc.*) and the properties of the liquid (concentration and species of ions, evaporation rate, *etc.*), whereas thermoelectric systems directly convert temperature gradients into electricity, enabling operation across diverse environments and offering greater adaptability.[51] Compared to photovoltaic technology, which is highly dependent on sunlight intensity and requires complex semiconductor materials, thermoelectric generators can function continuously as long as a thermal gradient is maintained, enhancing reliability and consistency.[52] Additionally, piezoelectric systems require mechanical deformation to generate electricity, limiting their scalability, whereas thermoelectric generators can be easily integrated into various applications, from small-scale wearable devices to large-scale energy harvesting setups.[53] Through the Seebeck effect, thermoelectric generators (TEGs) convert low-level heat into electrical energy by leveraging the temperature difference between a high-temperature steam generator and low-temperature bulk water. With relatively simple material requirements and the ability to utilize waste heat, thermoelectric power generation presents a promising and efficient approach for sustainable solar-driven water–energy cogeneration.

In conventional SG-TEG hybrid devices, the SG unit is typically positioned at the top of the TEG unit (Fig. 1a). The SG generates heat through photothermal conversion, serving as the hot end of the TEG, while the cold end of TEG is in direct contact with bulk water, dissipating heat into the surrounding medium.[54–58] In this concept, the heat generated by photothermal conversion transfers to the bulk water during evaporation, resulting in significant conductive heat loss. This, in turn, reduces the photothermal conversion efficiency and lowers the evaporation rate. Furthermore, heat transfer to the bulk water unavoidably increases the temperature at the cold end, diminishing the temperature differential across the TEG and thereby reducing electricity generation. Recent studies have addressed this issue by introducing circulating cooling water at the cold end of the TEG to maintain the temperature differential and enhance power generation in SG-TEG devices.[59–62] However, this approach can also carry away the residual heat from the SG, leading to a significant reduction in water evaporation rates.[63,64] Despite advancements, conventional setups often fall short in performance. This evaporation rate is generally lower than 2.0 kg m^{-2} h^{-1}, and long-term stable thermoelectric power generation is challenging. Hence, achieving both high-performance interfacial evaporation and stable thermoelectric power generation simultaneously remains a challenge for SG-TEG hybrid devices. In particular, optimizing the waste heat and environmental energy utilization of solar-driven water–electricity cogeneration hybrid devices has proven to be a formidable task.

In this work, we have proposed a "cold" evaporation cooling strategy to boost synergistic water–electricity cogeneration. To modulate the cold evaporation cooling effect, a heatsink-like SG fabricated using direct ink writing was integrated with a TEG to form the hybrid device. Unlike conventional SG-TEG hybrid systems that use bulk water for cooling, our strategy improved energy exchange between the thermoelectric generation component and the photothermal evaporation component by introducing a cold evaporation surface. This innovation enhanced environmental energy input and eliminated heat conduction losses to bulk water (Fig. 1b). Owing to the intricate structure enabled by 3D printing, the TEG can be easily embedded within the heatsink-like SG to form the integrated device. The SG transfers heat to the hot side of the TEG through photothermal conversion, while the cold evaporation surface dissipates heat for the TEG's cold side. On the one hand, the heatsink-like heat transfer channel enhances the evaporation cooling effect to dissipate heat from the cold end, thereby maintaining a stable temperature difference and ensuring long-term stable power generation performance. On the other hand, the heatsink-like design expands the cold evaporation surface area, increasing environmental energy intake and further promoting water evaporation rate. Under 1 sun (AM 1.5G), the heatsink-like SG-TEG hybrid device achieves an evaporation rate of 2.65 kg m^{-2} h^{-1}, which is, to the best of our knowledge, among the highest water evaporation rates reported for SGs. The maximum power density of the hybrid device also reaches 0.19 W m^{-2}. Regarding its long-term functionality, a key highlight is that the thermoelectricity performance remains stable for up to 8 h of testing without the use of recirculating condensed water. With all the above-mentioned results, this study simultaneously achieves efficient interfacial evaporation and stable thermoelectric power generation, offering a new paradigm for the integrated design of hybrid systems for high-performance water–electricity cogeneration.

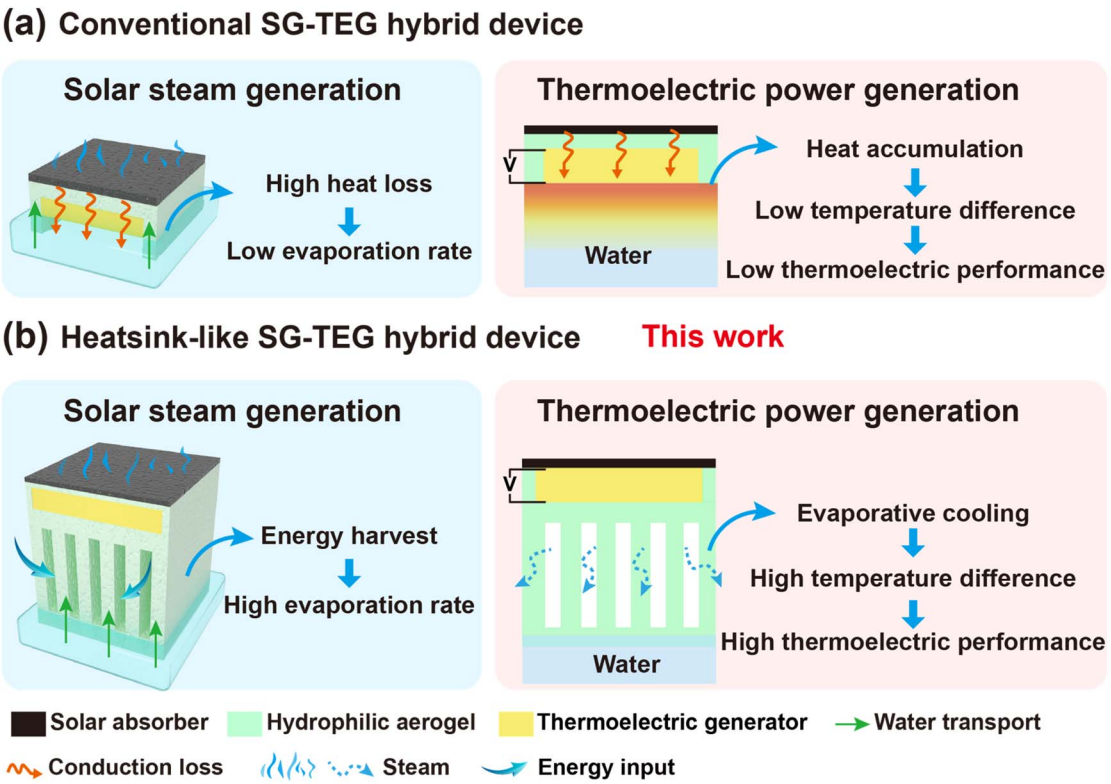

Fig. 1 Schematic illustration of synergistic interfacial evaporation and thermoelectric power generation based on (a) a conventional SG-TEG hybrid device and (b) a heatsink-like SG-TEG hybrid device.

2. Results and discussion

2.1 3D printing and characterization of aerogel matrices

The printing ink was composed of two components, including bacterial cellulose (BC, 3.0 wt%) as the primary structural material and glutaraldehyde (GA, 20 mg g^{-1}) as the cross-linking agent. Cellulose nanofibers (CNFs) prepared by bacteria exhibit higher crystallinity, and superior water absorption capacity and mechanical strength compared to plant-derived CNFs.[65,66] A large number of hydroxyl groups on the glucose units impart strong hydrophilicity, allowing for uniform dispersion in water. Meanwhile, the abundant hydrogen bonds within and between the molecular chains, as well as the entanglement between fibers, contribute to the appropriate viscosity for printing. These highly reactive hydroxyl groups on the CNFs offer a multitude of binding locations for chemical cross-linking after 3D printing.[67,68] The process for constructing a heatsink-like SG-TEG hybrid device is depicted in Fig. 2a. The model was built using computer-aided prototyping and manufactured by sequentially depositing printing ink. At a pressure range of 3.0–3.5 psi, the printing ink was extruded uniformly through a nozzle (diameter: 0.4 mm). The well-formed microfilaments were then stacked layer-by-layer to construct a 3D structure with negligible distortion during the printing process. At a printing speed of 15 mm s^{-1}, a heatsink-like aerogel with dimensions of $3 \times 3 \times 4$ cm^3 can be printed in 3 h. Subsequently, the 3D architecture was subjected to freeze-drying and heating, whereby the hydroxyl groups on CNFs reacted with the aldehyde groups of the GA to form covalent connections. Meanwhile, the *in situ* polymerization of polypyrrole (PPy) formed a solar absorber on the top surface of the aerogel. The chemical structures of the CNF and CNF/PPy were characterized using FTIR spectroscopy (Fig. S1, ESI†). The CNF presented the characteristic signals of O–H stretch, C–H stretch and C–O stretch at 3342, 2894 and 1055 cm^{-1}, respectively. CNF/PPy mainly showed characteristic peaks of PPy, with peaks at 1540 and 1448 cm^{-1} attributed to symmetrical stretching vibration of C=C on the pyrrole ring and C–N stretching vibration. The absorption peak at 1305 cm^{-1} corresponded to C–C stretching vibrations, and the absorption peak at 1161 cm^{-1} was assigned to C–H in-plane bending vibration. Additionally, the peak at 783 cm^{-1} represented the characteristic absorption of the pyrrole ring with an α–α connection, specifically corresponding to C–H out-of-plane bending vibrations at the β position of the pyrrole ring. These findings confirm the successful polymerization of pyrrole and the formation of the CNF/PPy composite. Finally, the TEG was embedded into the precise structure of the aerogel to assemble the heatsink-like SG-TEG hybrid device.

The rheological properties of the printing ink play a critical role in extrusion-based 3D printing. Ideally, the printing ink should be facilely extrudable through a narrow nozzle at an optimal pressure, while maintaining its structural integrity after deposition.[69,70] The plot of shear viscosity of the ink against

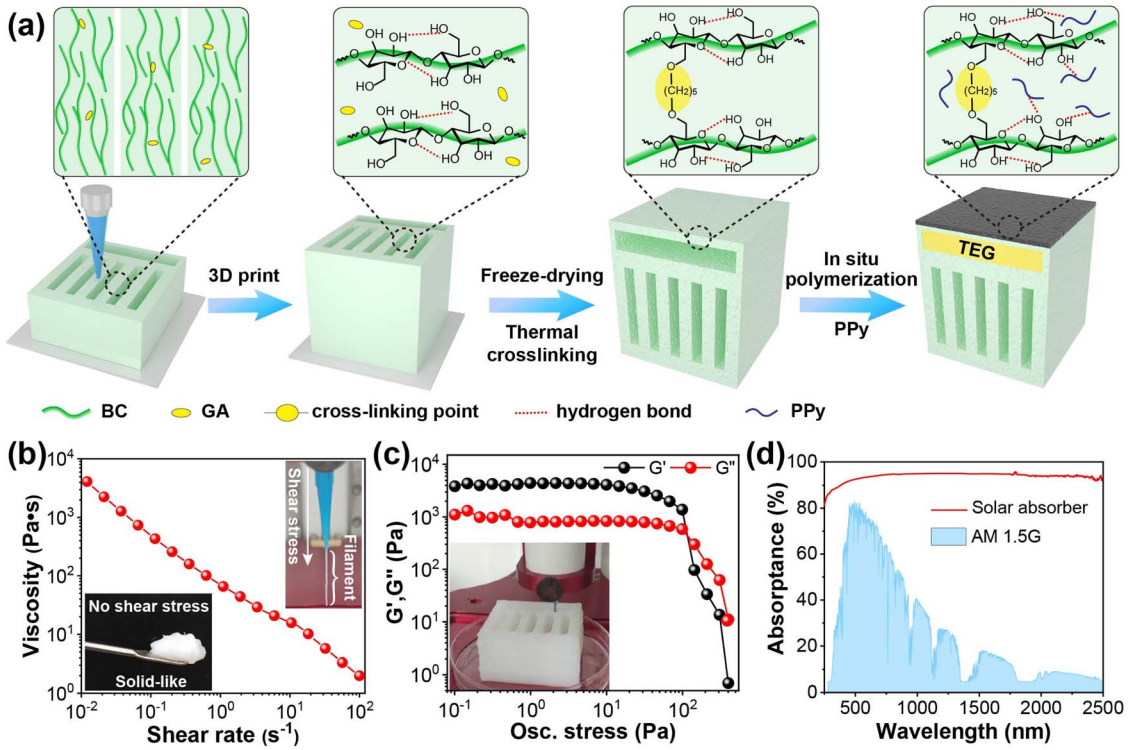

Fig. 2 (a) A flow chart of the fabrication of a heatsink-like SG-TEG hybrid device. (b) Shear viscosity of the printing ink under shear rate sweep (the inset images show the printing inks with and without shear stress). (c) Rheological properties of the printing ink: G' and G'' under oscillation stress sweep (the inset image shows the 3D printed model). (d) Absorbance spectrum of the CNFs/PPy composite aerogel.

shear rate, as illustrated in Fig. 2b, displays characteristic non-Newtonian behavior of shear-thinning. As the shear rate increased from 10^{-2} to 10^{2} s^{-1}, its viscosity decreased from 4115 to 2 Pa s. The inset shows that the printing ink exhibits a solid-like behavior in the absence of shear stress. It can dramatically transform into a liquid-like state under increased shear stress, allowing the printing ink to extrude smoothly through the print nozzle to form continuous microfilaments. In addition, the storage modulus (G') and loss modulus (G'') of the photo-thermal ink *versus* shear stress are shown in Fig. 2c. The printing ink exhibited viscoelastic behavior, with G' being an order of magnitude higher than G'' over a shear stress range of 10^{-1} to 10^{2} Pa. However, as the shear stress approached 10^{2} Pa, G' dropped sharply below G'', indicating that the printing ink transitioned to a predominantly viscous state. Rheological tests demonstrate that the printing ink composed of CNFs and GA is suitable for extrusion-based 3D printing. Besides, the solar absorption capability of the heatsink-like SG-TEG hybrid device is of great importance for its application as a solar-driven steam generator for water–electricity cogeneration. As shown in Fig. 2d, the solar absorbers feature a broad absorbance of 96% in the range of 250–2500 nm, benefiting from the strong light absorption properties of PPy.

The digital photograph in Fig. 3a illustrates the integration of the TEG with the heatsink-like aerogel, forming the SG-TEG hybrid device. The surface and cross-sectional morphology of the heatsink-like SG-TEG hybrid device were characterized using a macro camera and a Scanning Electron Microscope (SEM). The macro photograph revealed the formation of oriented microfilaments on the surface of the heatsink-like SG-TEG hybrid device, aligned parallel to the printing direction (Fig. 3b, left). The average width of the microfilaments was ~380 μm, slightly smaller than the nozzle diameter (400 μm), due to slight shrinkage during the freeze-drying and cross-linking processes. The local SEM image of the microfilaments depicts a light-trapped structure with highly porous morphology, which enhances light absorption (Fig. 3b, right). Energy-dispersive X-ray spectroscopy (EDS) analysis demonstrates that nitrogen atoms (N) were equally distributed throughout the solar absorber, confirming the homogeneous coating of PPy (Fig. 3c). A cellular structure with numerous open cells was observed in the cross-section perpendicular to the printing direction (Fig. 3d). Meanwhile, vertically arranged microchannels (average diameter: ~110 μm) with low tortuosity were also found in the cross-section parallel to the printing direction (Fig. 3e, left). The oriented microchannels with low tortuosity are formed during the 3D printing process, where the voids between the aligned microfilaments create a structured pathway. Subsequent freeze-drying and cross-linking steps preserve this aligned microstructure, resulting in continuous and well-defined microchannels. The low-tortuosity microchannels significantly reduce resistance to fluid flow and vapor diffusion, enabling efficient mass transport and rapid evaporation rates. Additionally, the aligned microfilaments create

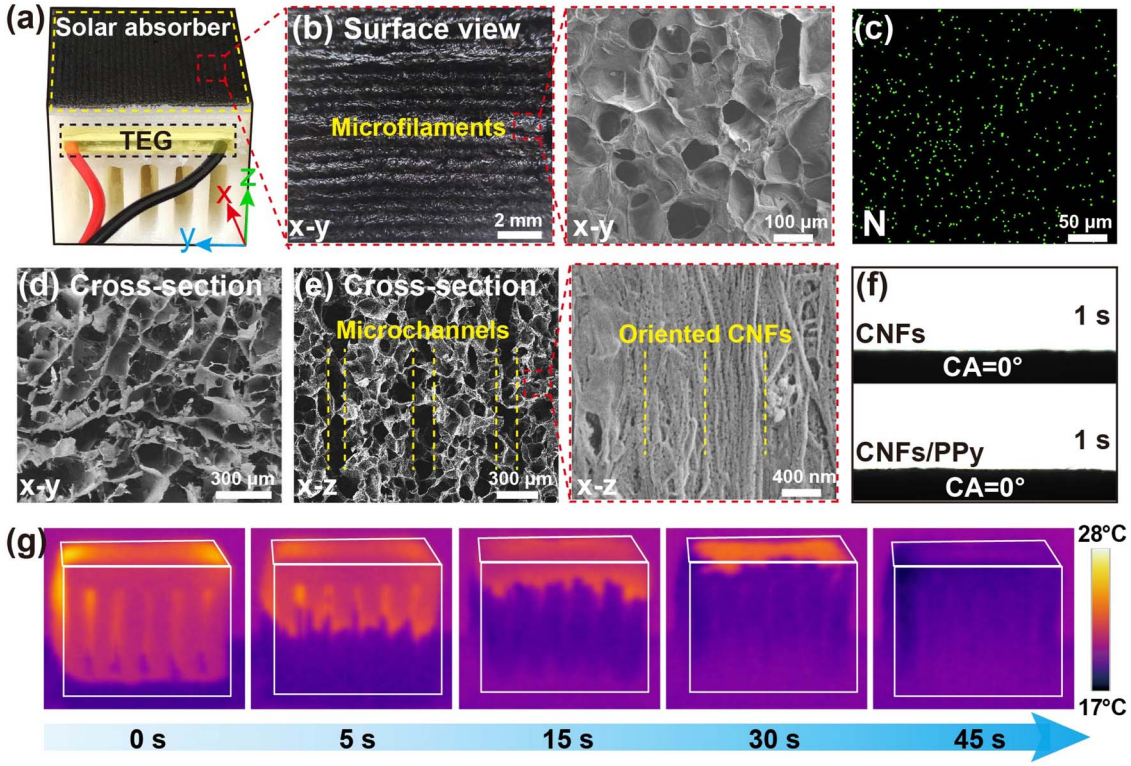

Fig. 3 (a) Digital photograph of the heatsink-like SG-TEG hybrid device. (b) Surface macro photograph (left) and a local SEM image (right). (c) EDS image of the characteristic element. (d) SEM images of the transverse cross-sections. (e) SEM images of the longitudinal cross-sections. (f) Surface contact angle measurements. (g) Water diffusion characterization over 45 s.

a continuous and structured pathway for heat conduction, improving thermal management by facilitating uniform heat distribution and dissipation. The high-resolution SEM image reveals the orientation of the CNFs in the microfilaments along the printing direction (Fig. 3e, right). Water contact angle measurements show that water droplets were readily absorbed within 1 s on the surfaces of CNFs and CNFs/PPy, indicating the superhydrophilicity of both the solar absorbers and heat transfer channels (Fig. 3f). Finally, the bottom-up water transport of the heatsink-like SG-TEG hybrid device (4 cm in height) was characterized *via* an infrared (IR) camera (Fig. 3g). Owing to the high hydrophilicity of the CNFs and the strong capillary effect of the highly porous structure, water could be rapidly transported to the top of the heatsink-like SG-TEG hybrid device, reaching a height of 4 cm within a short time of ~45 s. Such a heatsink-like SG-TEG hybrid device exhibited fast water transport and excellent water resistance, with no significant deformation upon wetting with water, providing the basis for a sufficient water supply and long-term stable evaporation.

2.2 Solar evaporation characterization

A conventional SG-TEG hybrid device (named SG-TEG-1) was prepared through 3D printing with the same ink, which served as the control group (Fig. 4a). In this typical device structure, the SG was positioned above the TEG, generating heat through photothermal conversion and serving as the hot end of the TEG, while the cold end of the TEG was in direct contact with the water surface. On the other hand, the delicate 3D-printed structure allows the TEG to be assembled with the heatsink-like SG, with the solar absorber acting as the hot end and the cold evaporation surface as the cold end. By adjusting the water level, the height of the cold evaporation surface of SG-TEG-2 exposed to air could be fixed at 0.5, 1, 2, and 3 cm. Indoor solar evaporation measurements were performed using an artificial optical setup (solar intensity: AM 1.5G, 0.8–2 kW m^{-2}, room temperature: 25.0 °C, and relative humidity: 60%). The substantial heat loss and the limited effective evaporation area resulted in a low evaporation rate of SG-TEG-1, which was only 1.30 kg m^{-2} h^{-1} under 1 sun illumination (AM 1.5G, 1 kW m^{-2}). For SG-TEG-2, increasing the height of the cold evaporation surface from 0.5 cm to 3 cm significantly expanded the effective evaporation area, resulting in an increase in the evaporation rate from 1.65 kg m^{-2} h^{-1} to 2.65 kg m^{-2} h^{-1} (Fig. 4b and c). It is evident that the heatsink-like structure of SG-TEG-2 yields significantly superior water evaporation in comparison to SG-TEG-1 with a planar structure. To further evaluate water evaporation of SGs under different solar irradiation conditions, the height of the cold evaporation surface of SG-TEG-2 was fixed at 3 cm, and the evaporation rates of SG-TEG-1 and SG-TEG-2 were tested under 0.8, 1, and 2 kW m^{-2} irradiation, respectively. The performance of both SG-TEG-1 and SG-TEG-2 enhanced significantly with the increase of solar irradiation (Fig. 4d and e). The evaporation rates of SG-TEG-1 under 0.8, 1, and 2 kW m^{-2} irradiation were 1.02, 1.30, and 1.74 kg m^{-2} h^{-1}, respectively.

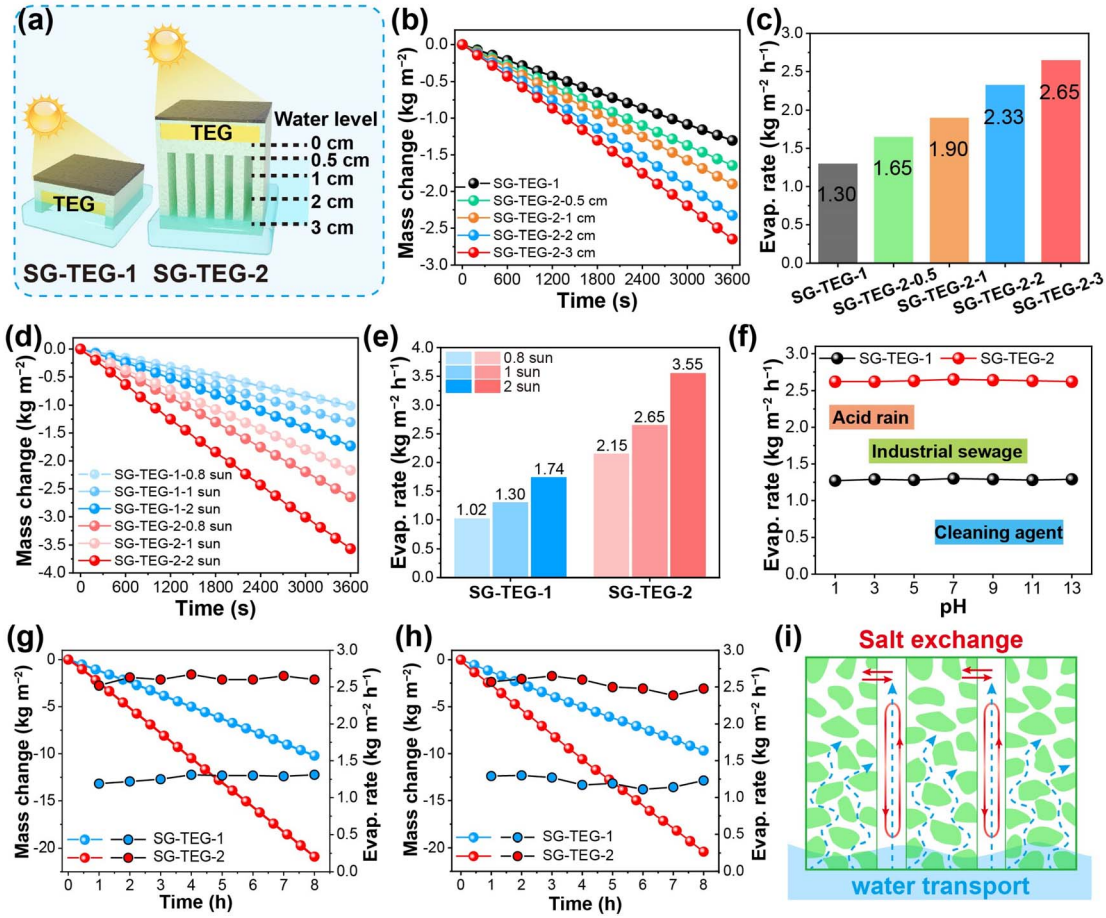

Fig. 4 (a) Schematic illustration of SG-TEG-1 and SG-TEG-2. (b) Mass changes and (c) summary of water evaporation rates under 1 sun. (d) Mass changes and (e) summary of water evaporation rates under different solar irradiation conditions. (f) Water evaporation rates of SG-TEG-1 and SG-TEG-2 over a wide range of pH. Solar desalination of SG-TEG-1 and SG-TEG-2 in (g) 3.5 wt% and (h) 10 wt% brine. (i) Schematic illustration of the salt-exchange mechanism.

Under the same conditions, SG-TEG-2 exhibited relatively higher evaporation rates of 2.15, 2.65 and 3.55 kg m^{-2} h^{-1}, respectively. Evidently, SG-TEG-2 outperforms SG-TEG-1 in both weak and intense light exposure, exhibiting a high evaporation rate among high-performance SGs.

In fact, a porous structure and high specific surface area are the key features of aerogels. However, in most aerogel-based interfacial SGs, the pores become saturated with water and cannot effectively participate in steam generation, functioning only as pathways for water diffusion. Consequently, solar interfacial evaporation occurs solely on the external surface of SG-TEG-1. By adopting a heatsink-like structure based on 3D-printed aerogel matrices, the internal surfaces of the SG-TEG-2 are open to air, enabling them to participate in the evaporation process. Furthermore, the effective evaporation areas of SG-TEG-1 and SG-TEG-2 with different cold evaporation surface heights were compared. For SG-TEG-1, the effective evaporation area was measured to be the smaller value of 29 cm^2 (Fig. S2, ESI†). In contrast, the internal surface of SG-TEG-2 was exposed to air, profiting from the 3D-printed heatsink-like structure, which significantly expanded the effective evaporation area. Hence, the effective evaporation area of the SG-TEG-2 gradually increased with the height of the cold evaporation surface. Accordingly, when the cold evaporation surface height reached 3 cm, the effective evaporation area of SG-TEG-2 extended to 251 cm^2, representing an 8.6-fold increase compared to that of SG-TEG-1. These results underscore a significant advantage of the heatsink-like structure: it provides a substantially larger effective evaporation area than conventional aerogels, enhances environmental energy input for steam generation and facilitates water vapor release.

In this design, the 3D-printed aerogel displays oriented channels in which CNFs are also oriented along the printing path. To investigate the influence of orientation on heat transfer, the thermal conductivity of the SGs was evaluated by measuring the thermal conductivity of the 3D-printed aerogel in directions parallel and perpendicular to the printing path. Slightly higher thermal conductivities (0.35 W m^{-1} K^{-1} for the dry state and 0.48 W m^{-1} K^{-1} for the wet state) were obtained for the aerogel parallel to the printing direction, while the thermal conductivities (0.30 W m^{-1} K^{-1} for the dry state and 0.40 W m^{-1} K^{-1} for the wet state) of the aerogel perpendicular to

the printing direction were lower (Fig. S3, ESI†). This result indicates that heat from sunlight and surrounding air can be effectively transferred through the microfibers within the SG.

Based on variations in the absorbance, surface temperature, ambient temperature, and water temperature, calculations were conducted to determine the energy loss and input for SG-TEG-1 and SG-TEG-2. Both devices exhibited the same reflective loss of 4% owing to the identical composition and morphology of the photothermal conversion layer (Fig. S4, ESI†). The difference in surface temperature and thermal evaporation surface area led to slightly lower radiative and convective heat losses for SG-TEG-1 (5.3% and 4.0%) compared to those for SG-TEG-2 (9.7% and 7.4%). However, the direct contact of the TEG in SG-TEG-1 with water caused a significant conductive heat loss of 13.0%. In contrast, the heatsink-like design of SG-TEG-2 completely eliminated conductive heat loss, with no measurable loss. Regarding energy intake, the planar structure of SG-TEG-1 rendered it devoid of a cold evaporation surface, making it incapable of absorbing energy from the surrounding environment. Conversely, SG-TEG-2 displayed an expanded cold evaporation surface attributed to the heatsink-like design, enabling 52.6% energy input *via* ambient radiation and convection. In total, SG-TEG-1 exhibited a heat loss of 26.3% with no energy intake, while SG-TEG-2 showed a heat loss of 21.1% coupled with an energy intake of 52.6%. It is evident that the heatsink-like structure of SG-TEG-2 reduces heat dissipation and enhances energy harvesting, which is the primary driver of its elevated evaporation rate.

In dark environments, ambient energy input serves as the sole energy source for the SG. SG-TEG-1 exhibited a subdued dark evaporation rate of 0.11 kg m^{-2} h^{-1} due to its limited effective evaporation area (Fig. S5, ESI†). In contrast, the effective evaporation area of SG-TEG-2 expanded progressively as the height of the cold evaporation surface increased, resulting in an enhanced dark evaporation rate. When the height of the cold evaporation surface reached 3 cm, the dark evaporation rate attained a value of 0.37 kg m^{-2} h^{-1}, which was 3.3 times higher than that of SG-TEG-1 (Fig. S5, ESI†). Thus, it can be concluded that SG-TEG-2 holds a distinct advantage in leveraging ambient energy to facilitate evaporation. The cold evaporation cooling strategy optimizes waste heat recovery from the hybrid module and ambient energy utilization, minimizes thermal conduction losses and enhances environmental energy intake, thereby achieving a high evaporation rate.

To verify the practical potential of SGs, the evaporation performance of SG-TEG-1 and SG-TEG-2 was tested in wastewater with various pH values. Under 1 sun illumination, the evaporation rates of SG-TEG-1 in wastewater with pH values of 1, 3, 5, 9, 11, and 13 were recorded at 1.27, 1.29, 1.28, 1.29, 1.28, and 1.29 kg m^{-2} h^{-1}, respectively (Fig. 4f and S6, ESI†). Comparatively, SG-TEG-2 exhibited evaporation rates of 2.62, 2.62, 2.63, 2.64, 2.63, and 2.62 kg m^{-2} h^{-1}, respectively. Both SG-TEG-1 and SG-TEG-2 maintained stable evaporation rates in acidic and alkaline wastewater, comparable to those observed in pure water. The results indicate that the composition and structure of SGs remained stable under acidic and alkaline conditions, demonstrating robust acid-alkali resistance. Significantly, the low thermal conduction loss and high environmental energy input enable SG-TEG-2 to exhibit a significantly enhanced evaporation performance compared to SG-TEG-1 across a broad pH range.

Meanwhile, long-term solar desalination was characterized by placing SG-TEG-1 and SG-TEG-2 in brine solutions with varying salinities. Under 1 sun, both SG-TEG-1 and SG-TEG-2 maintained stable evaporation rates of 1.28 and 2.63 kg m^{-2} h^{-1}, respectively, for a continuous 6 h in 3.5 wt% saline solution (Fig. 4g). After 6 h of brine evaporation, the surfaces of SG-TEG-1 and SG-TEG-2 remained clean, without any salt deposition (Fig. S7, ESI†). As the saltwater concentration increased to 10 wt%, both SG-TEG-1 and SG-TEG-2 still held stable evaporation rates for a continuous 6-hour period under 1 sun illumination, with average evaporation rates recorded at 1.20 and 2.54 kg m^{-2} h^{-1}, respectively. Also, no salt deposition occurred on the surfaces of SG-TEG-1 and SG-TEG-2 after 6 h of evaporation (Fig. 4h). These results demonstrate that both SG-TEG-1 and SG-TEG-2 exhibit excellent salt tolerance during solar desalination processes, which is attributed to the hydrophilicity of the materials and the rapid water transport capabilities enabled by oriented channels. The low-curvature channels constructed through 3D printing significantly enhance capillary action, accelerating water transport (Fig. 4i). This allows the salt accumulated at the top of the SGs to redissolve into the bulk water, preventing solid salt deposition on the surface of the SGs and thereby enhancing salt resistance. Consequently, the developed heatsink-like SG achieves continuous and stable solar desalination, showcasing its outstanding anti-fouling properties across a wide range of saline water conditions.

2.3 Thermoelectricity generation characterization

To evaluate the device performance in detail, temperature distributions within SG-TEG-1 (Fig. 5a) and SG-TEG-2 (Fig. 5b) at different cold evaporation surface heights were measured using thermocouples. The surface temperature (T_1) of SG-TEG-1 gradually increased and stabilized at 38.1 °C after 1 h of sunlight exposure (Fig. S8a, ESI†). As heat gradually transferred, the temperature of the TEG's hot end (T_2) and cold end (T_3, water temperature) increased along with T_1, stabilizing at 37.1 °C and 35 °C, respectively. On the other hand, the T_1 of SG-TEG-2 with a cold evaporation surface height of 0.5 cm (SG-TEG-2-0.5) increased to 38 °C after 1 h of exposure, while T_2 and T_3 increased and stabilized at 37.1 and 34.8 °C, respectively (Fig. S8b, ESI†). Over the course of 8 h of continuous testing, the water temperature (T_4) increased from 24.3 to 27.8 °C.

Furthermore, when the cold evaporation surface height of SG-TEG-2 increased to 1, 2, and 3 cm (SG-TEG-2-1, SG-TEG-2-2, and SG-TEG-2-3), T_1 and T_2 of SG-TEG-2 both rose to 38 and 37 °C, respectively, while T_3 stabilized at 34.3, 33.0, and 33.0 °C. In this process, the water temperature (T_5, T_6, and T_7) increased from 24.3 °C to 27.6, 24.7, and 24.9 °C, respectively (Fig. S8c–e, ESI†). Notably, T_6 was lower than T_7, indicating that the heat from the evaporation module of SG-TEG-2-3 had been completely consumed before reaching the site of T_6. The evaporative cooling effect resulted in T_6 being lower than the water

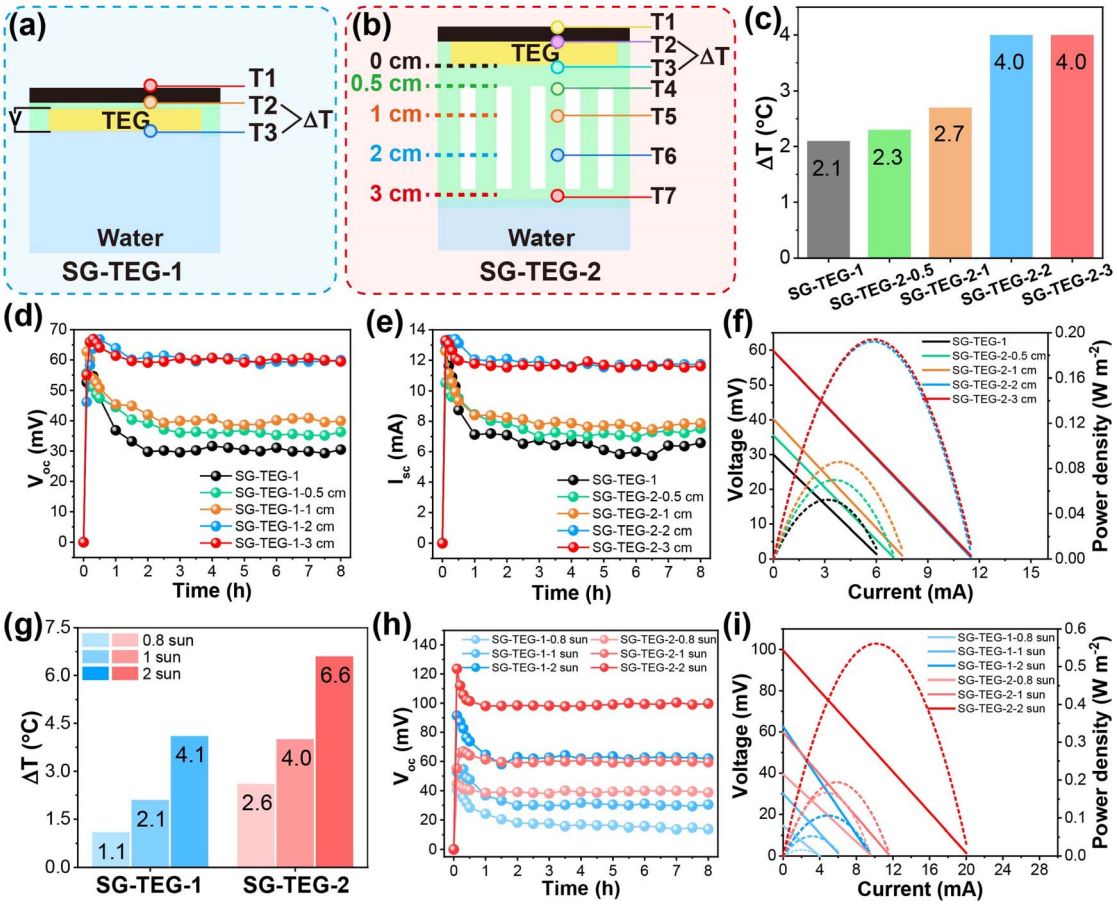

Fig. 5 Schematic illustration of (a) SG-TEG-1 and (b) SG-TEG-2. (c) The temperature difference of SG-TEG-1 and SG-TEG-2 under 1 sun. (d) V_{oc} of SG-TEG-1 and SG-TEG-2 under 1 sun. (e) I_{sc} of SG-TEG-1 and SG-TEG-2 under 1 sun. (f) The corresponding power density under 1 sun. (g) The temperature difference of SG-TEG-1 and SG-TEG-2 under different solar irradiation conditions. (h) V_{oc} of SG-TEG-1 and SG-TEG-2 under different solar irradiation conditions. (i) The corresponding power density under different solar irradiation conditions.

temperature. From this, it can be inferred that when the cold evaporation surface height of the SG reaches or exceeds 2 cm, evaporation could be maximized to cool the TEG's cold end. After statistical calculations, it was found that the temperature difference between the hot end and cold end of the TEG in SG-TEG-1 was 2.1 °C (Fig. 5c and S8f, ESI†). For SG-TEG-2, the temperature difference increased from 2.3 °C to 4.0 °C as the cold evaporation surface height increased from 0.5 cm to 2 cm. No further increase in ΔT was observed when the height was raised to 3 cm.

To assess the long-term water–electricity cogeneration of the hybrid devices, open-circuit voltage (V_{oc}), short-circuit current (I_{sc}) and power density of SG-TEG-1 and SG-TEG-2 with different cold evaporation surface heights were measured under continuous illumination for 8 h. It can be observed that the V_{oc} of SG-TEG-1 rapidly increased to 55 mV and then gradually decreased, eventually stabilizing at 30 mV (Fig. 5d). The heat transfer from SG-TEG-1 to the bulk water elevated the cold end temperature of the TEG, resulting in a reduction in the temperature difference, thus leading to a significant decrease in V_{oc}. For SG-TEG-2, as the cold evaporation surface height increased, the magnitude of the V_{oc} decline gradually diminished. When the height increased to 2 and 3 cm, the V_{oc} stabilized at 60 mV during the continuous 8-hour testing, twice that of SG-TEG-1. The trend in I_{sc} variation was similar to that of V_{oc}. The I_{sc} of SG-TEG-1 rapidly increased to 12 mA and finally stabilized at 6.2 mA (Fig. 5e). In comparison, the I_{sc} of SG-TEG-2 stabilized at 11.8 mA during the long-term measurements upon the cold evaporation surface height reaching 2 and 3 cm. As summarized in Fig. 5f, the maximum power density of SG-TEG-1 was about 0.052 W m^{-2}, while the maximum power density of SG-TEG-2-0.5, SG-TEG-2-1, SG-TEG-2-2, and SG-TEG-2-3 was 0.07, 0.086, 0.19 and 0.19 W m^{-2} under 1 sun, respectively. These results demonstrate that the heatsink-like design of SG-TEG-2 effectively dissipates heat for the cold end of the TEG by leveraging the cold evaporation cooling strategy. This design utilizes the cold evaporation area for cooling the TEG's cold end, ensuring a stable temperature difference between the two ends of the TEG, thus maintaining continuous and stable power generation over an extended period.

As the final key indicator of this hybrid device's performance, the electricity generation was measured under various solar intensities. The cold evaporation surface height of SG-TEG-2 was fixed at 3 cm, the temperature difference and electricity

generation performance of SG-TEG-1 and SG-TEG-2 were tested under solar irradiation of 0.8, 1, and 2 kW m^{-2} (equivalent to 0.8, 1, and 2 suns). With the increase in solar irradiation, the temperature difference between the hot and cold ends of the TEG in both SG-TEG-1 and SG-TEG-2 significantly increased (Fig. S9, ESI†). Under solar irradiation of 0.8, 1, and 2 kW m^{-2}, the temperature differences for SG-TEG-1 were 1.1, 2.1, and 4.1 °C, respectively, whereas SG-TEG-2 exhibited relatively higher values of 2.6, 4.0, and 6.6 °C, respectively (Fig. 5g). Besides, the V_{oc} of SG-TEG-1 for 8 h of continuous testing under solar irradiation of 0.8, 1 and 2 kW m^{-2} was 13.5, 30, and 62 mV, respectively, while the V_{oc} of SG-TEG-2-3 was 39.5, 60, and 99.5 mV, respectively (Fig. 5h). The measured I_{sc} values for SG-TEG-1 were 4.2, 6.4, and 9.6 mA, whereas SG-TEG-2-3 displayed I_{sc} of 9.8, 11.5, and 20.4 mA (Fig. S10, ESI†). As a result, the maximum power density of SG-TEG-1 was about 0.016, 0.052, and 0.17 W m^{-2}, respectively, while that of SG-TEG-2-3 was 0.11, 0.19, and 0.56 W m^{-2}, respectively (Fig. 5i and Table S1, ESI†). This clearly shows that SG-TEG-2 demonstrates a significant advantage under both weak and intense sunlight. The results indicate that the heatsink-like design and CEC strategy in this study have enhanced the thermoelectricity generation of the SG, enabling continuous and stable power generation without the need for additional circulating cooling water. The high evaporation rate and long-term stability of power generation performance of SG-TEG-2 rank it among the best-performing water–electricity cogeneration devices reported to date (Table S2 and Fig. S11, ESI†). This demonstrates the effectiveness of the cold evaporation cooling strategy implemented through the heatsink-like structure, which synergistically utilizes waste heat from the hybrid module and ambient energy.

3. Conclusion

In summary, we have presented a CEC strategy for constructing a novel solar-driven water–energy cogeneration device to achieve optimal efficiency in both green power and clean water production. By utilizing 3D printing technology, a heatsink-like interfacial SG was successfully constructed and employed for water–energy cogeneration, balancing high-performance interfacial evaporation and stable thermoelectric power generation. The specific conclusions are as follows: (i) based on the regulation of printing inks, a heatsink-like interfacial SG was fabricated *via* 3D printing, achieving efficient photothermal conversion, directional water transport, energy management, salt resistance, and water–energy cogeneration in a synergistic manner. (ii) The heatsink-like design expanded the cold evaporation surface area of the interface SG, enhancing the environmental energy intake and further promoting evaporation performance. Under 1 sun, a high evaporation rate of 2.65 kg m^{-2} h^{-1} was achieved, ranking among the best-performing solar-powered interfacial SGs. The construction of low-curvature oriented channels within the SG significantly enhanced the capillary action, facilitating water transport, strengthening the salt tolerance of the interfacial SG, and achieving long-term stable solar desalination. (iii) The heatsink-like SG-TEG hybrid device was constructed by integrating the TEG with SG, which leverages the cold evaporation cooling effect to dissipate heat from the TEG's cold side, maintaining a stable temperature difference across the TEG. Under 1 sun, it achieved a maximum power density of 0.19 W m^{-2}, about 365% higher than that of the conventional hybrid device. It also demonstrated stable thermoelectric performance under both low and high irradiance conditions, enabling efficient interfacial evaporation and consistent power generation for high-performance water–electricity cogeneration. This work introduces a novel strategy for the design of water–energy cogeneration devices tailored for customized applications.

4. Experimental section

4.1 Preparation of the printing ink

The BC suspension (0.8 wt%) was placed into dialysis bags and immersed in a PEG-20000 solution (15 wt%) until the concentration increased to 3.0 wt%. 200 mg of GA (50 wt% in water) was added into 10 g of the BC suspension (3.0 wt%) and mixed using a homogenizer to form the printable ink.

4.2 Preparation of 3D-printed aerogel matrices

The 3D structures were modeled using Materialise Magics. The printing ink was loaded into a syringe (10 mL) and printed using an Allevi 2 bioprinter through a nozzle (diameter: 0.4 mm) at a printing speed of 15 mm s^{-1}. The ink extrusion was controlled using a syringe pump with a pressure of 3.5 psi. The printed 3D structure was freeze-dried and heated to 80 °C for 2 h.

4.3 *In situ* polymerization of PPy

The $FeCl_3 \cdot 6H_2O$ solution (1 mol L^{-1}) and pyrrole solution (0.2 mol L^{-1}) were coated on the upper surface of the 3D printed aerogel. After being left for 2 h at room temperature, the PPy photothermal layer was formed on the surface of the SGs.

4.4 Solar evaporation measurements

Indoor solar evaporation experiments were conducted using a xenon lamp (CEL-S500, CEAULIGHT) with an AM 1.5G optical filter at a room temperature of ~25 °C and a relative humidity of ~60%. The solar flux was calibrated using a thermopile connected to a power meter (CEL-NP2000, CEAULIGHT). The water's mass changes were recorded in real time by using a high-precision electronic balance (QUINTIX224-1CN, Sartorius, accuracy: 0.1 mg). The temperature distribution of the systems was monitored using an IR camera (223s-L19, Fotric Precision Instruments) and k-type thermocouples.

Data availability

The data supporting this article have been included as part of the ESI.†

Conflicts of interest

The authors declare no competing financial interest.

Acknowledgements

The authors acknowledge the financial support from the National Natural Science Foundation of China (Grant No. 22379133), the Taishan Scholar Program of Shandong Province, China (Grant No. tsqn201812026), the Natural Science Foundation of Shandong Province, China (Grant No. ZR2023MB087 and ZR2022QE102), the Natural Science Foundation of Qingdao, China (Grant No. 23-2-1-243-zyyd-jch) and the Open Fund of the State Key Laboratory of Luminescent Materials and Devices, South China University of Technology (Grant No. 2023-skllmd-01).

References

1 P. Zhang, H. Wang, J. Wang, Z. Ji and L. Qu, *Adv. Mater.*, 2023, **36**, 2303976.
2 M. Yang, Y. Wu, M. Chen, Y. Wang, L. Zhang, Y. Deng, D. Ye, Y. Zhan, G. Xiao and X. Jiang, *Small*, 2024, **20**, 2402151.
3 Y. Liang, D. Wang, H. Yu, X. Wu, Y. Lu, X. Yang, G. Owens and H. Xu, *Sci. Bull.*, 2024, **69**, 3590.
4 X. Lu, C. Mu, Y. Liu, L. Wu, Z. Tong and K. Huang, *Nano Energy*, 2024, **120**, 109180.
5 J. Chen, X. Wang, B. Wang, T. Wu, L. Zhang, K. Zhang, G. Fang, Y. Wang, Y. Zhao and G. Yang, *Small*, 2024, **20**, 2403221.
6 B. Wang, X. Huang, Z. Liu, J. Zhang, C. Wei, B. Cai, P. Xie and A. Zhou, *Energy Environ. Sci.*, 2024, **17**, 7600.
7 L. Li, S. Feng, L. Du, Y. Wang, C. Ge, X. Yang, Y. Wu, M. Liu, S. Wang, Y. Bai, F. Sun and T. Zhang, *Nano Energy*, 2022, **99**, 107356.
8 T. A. Wani, P. Garg, P. Kaith and A. Bera, *J. Mater. Chem. A*, 2022, **10**, 21273.
9 S. Sun, H. Li, M. Zhang, B. Sun, Y. Xie, W. Zhou, P. Yang, H. Y. Mi, Z. Guo, C. Liu and C. Shen, *Small*, 2023, **19**, 2303716.
10 D. Zhang, Y. Wan, W. Zhuang, X. Geng and P. Yang, *Chem. Eng. J.*, 2023, **466**, 143047.
11 J. Su, Y. Xie, H. Zhao, Y. Xu, X. Lin, C. Shi, X. Cao and C. Wang, *Chem. Eng. J.*, 2024, **496**, 153764.
12 X. Lu, C. Mu, L. Nong, C. Lan, Z. Tong and K. Huang, *Chem. Eng. J.*, 2024, **496**, 154291.
13 A. Taranova, E. Moretti, K. Akbar, G. Dastgeer and A. Vomiero, *Nano Energy*, 2024, **128**, 109872.
14 T. Wang, M. Li, H. Xu, X. Wang, M. Jia, X. Hou, S. Gao, Q. Liu, Q. Yang, M. Tian, L. Qu, Z. Song, X. Wu, L. Wang and X. Zhang, *Nano–Micro Lett.*, 2024, **16**, 220.
15 H. Yu, H. Jin, M. Qiu, Y. Liang, P. Sun, C. Cheng, P. Wu, Y. Wang, X. Wu, D. Chu, M. Zheng, T. Qiu, Y. Lu, B. Zhang, W. Mai, X. Yang, G. Owens and H. Xu, *Adv. Mater.*, 2024, **36**, 2414045.
16 P. Yang, W. Bai, Y. Zou, X. Zhang, Y. Yang, G. Duan, J. Wu, Y. Xu and Y. Li, *Mater. Horiz.*, 2023, **10**, 1020.
17 R. Li, M. Wu, H. Ma, Y. Zhu, H. Zhang, Q. Chen, C. Zhang and Y. Wei, *Adv. Mater.*, 2024, 2402016.
18 H. Zhao, D. Shang, H. Li, M. Aizudin, H. Zhu, X. Zhong, Y. Liu, Z. Wang, R. Ni, Y. Wang, S. Tang, E. H. Ang and F. Yang, *Mater. Horiz.*, 2024, **11**, 5081.
19 L. Liu, H. Liu, Z. Fan, J. Liu, X. Wen, H. Wang, Y. She, G. Hu, R. Niu and J. Gong, *Energy Environ. Mater.*, 2024, e12812.
20 F. Li, N. Li, S. Wang, L. Qiao, L. Yu, P. Murto and X. Xu, *Adv. Funct. Mater.*, 2021, **31**, 2104464.
21 X. Zhang, M. Zhu, J. Chen, Z. Wang, S. Li, H. Yang, H. Xu, G. He, Z. Deng, S. Gu, X. Liu and B. Shang, *Mater. Horiz.*, 2024, **11**, 1779.
22 J. Dai, H. Wang, X. Yang, L. Lan, S. Li, G. Zhang, R. Li, D. Nie and W. Zhang, *Mater. Horiz.*, 2024, **11**, 2095.
23 Z. Gan, W. Sun, S. Zhao, Z. Zhang, H. Xie, X. Li, X. Li, P. Zhang, Y. Song, Y. Xia and Z. Yang, *Chem. Eng. J.*, 2024, **495**, 153694.
24 Y. Mi, Y. Li, Y. Tao, Y. Chen, J. Bai, G. Wang, L. Wang, S. Ma and B. Wang, *Chem. Eng. J.*, 2024, **496**, 153890.
25 L. Li, N. He, B. Jiang, K. Yu, Q. Zhang, H. Zhang, D. Tang and Y. Song, *Adv. Funct. Mater.*, 2021, **31**, 2104380.
26 Z. Wang, J. Gao, J. Zhou, J. Gong, L. Shang, H. Ye, F. He, S. Peng, Z. Lin, Y. Li and F. Caruso, *Adv. Mater.*, 2023, **35**, 2209015.
27 W. He, L. Zhou, Y. Wang, L. Yu, Y. Hou, S. Bi, M. Wang and X. Hou, *EcoMat*, 2023, **5**, 12355.
28 M. A. Abdelsalam, M. Sajjad, A. Raza, F. AlMarzooqi and T. Zhang, *Nat. Commun.*, 2024, **15**, 874.
29 Y. Zhang, Q. Zhong, Q. Huang, M. Hu, F. He, Y. Li and Z. Wang, *Adv. Funct. Mater.*, 2024, **34**, 2408554.
30 M. Liu, Y. Sun, K. Shao, N. Li, J. Li, P. Murto, Z. Wang, J. Chen and X. Xu, *Nano Energy*, 2024, **119**, 109074.
31 B.-L. Bai, S. Du and M.-J. Li, *Energy Convers. Manage.*, 2024, **302**, 118147.
32 W. Li, Z. Zheng, Z. Qian, H. Liu and X. Wang, *Adv. Funct. Mater.*, 2024, **34**, 2316504.
33 L. Li, C. Xue, Q. Chang, X. Ren, N. Li, J. Yang, S. Hu and H. Xu, *Adv. Mater.*, 2024, **36**, 2401171.
34 L. Chen, J. Ren, J. Gong, J. Qu and R. Niu, *Chem. Eng. J.*, 2023, **454**, 140383.
35 X. Cui, Q. Ruan, X. Zhuo, X. Xia, J. Hu, R. Fu, Y. Li, J. Wang and H. Xu, *Chem. Rev.*, 2023, **123**, 6891.
36 X. Wu, Y. Lu, X. Ren, P. Wu, D. Chu, X. Yang and H. Xu, *Adv. Mater.*, 2024, **69**, 2313090.
37 M. Ebrahimian Mashhadi, M. M. Hassan, R. Yang and Q. Lu, *Adv. Funct. Mater.*, 2024, **35**, 2412870.
38 Y. Chen, J. He, C. Ye and S. Tang, *Adv. Energy Mater.*, 2024, **14**, 2400529.
39 H. Liu, L. Liu, Z. Fan, J. Liu, H. Wang, X. Wen, G. Hu, K. Liu, R. Niu and J. Gong, *Chem. Eng. J.*, 2024, **485**, 149690.
40 G. Hu, H. Liu, K. Liu, H. Wang, X. Wen, L. Liu, Y. She, L. Feng, R. Niu and J. Gong, *Adv. Funct. Mater.*, 2025, **35**, 2423781.
41 H. Wang, X. Wen, K. Liu, Q. Liu, G. Hu, H. Liu, Y. She, R. Niu, T. Tang and J. Gong, *SusMat*, 2024, **4**, e242.
42 G. Huang, J. Xu and C. N. Markides, *Nat. Commun.*, 2023, **14**, 3344.

43 M. Wang, Y. Wei, X. Wang, R. Li, S. Zhang, K. Wang, R. Wang, H. Chang, C. Wang, N. Ren and S.-H. Ho, *Nat. Water*, 2023, **1**, 716.
44 J. Long, J. Yin, F. Yang, G. Zhou, H.-M. Cheng, W. Guo and L. Qiu, *Adv. Energy Mater.*, 2025, **15**, 2303476.
45 C. Cheng, J. Fang, Y. Chai, R. Yuan and H. Liu, *Chem. Eng. J.*, 2024, **498**, 155665.
46 S. Meng, C.-Y. Tang, J. Yang, M.-B. Yang and W. Yang, *Adv. Sci.*, 2022, **9**, 2204187.
47 C.-H. Huang, J.-X. Huang, Y.-H. Chiao, C.-M. Chang, W.-S. Hung, S. J. Lue, C.-F. Wang, C.-C. Hu, K.-R. Lee, H.-H. Pan and J.-Y. Lai, *Adv. Funct. Mater.*, 2021, **31**, 2010422.
48 J. Li, L. Wang, C. Zhang, H. Wang, Y. Pan, S. Li, X. K. Chen, T. Jia and K. Wang, *Angew. Chem., Int. Ed.*, 2024, **63**, e202402726.
49 Z. Mao, Y. Yao, J. Shen, J. Liu, Y. Chen, B. Zhou, Y. Chen, Q. Wang and J. Lu, *Nat. Water*, 2024, **2**, 93.
50 L. Zeng, D. Deng, L. Zhu, Z. Zhang, X. Gu, H. Wang and Y. Jiang, *Nano Energy*, 2024, **125**, 109531.
51 C. Ge, D. Xu, Y. Qian, H. Du, C. Gao, Z. Shen, Z. Sun and J. Fang, *Green Chem.*, 2023, **25**, 7470.
52 Z. Mao, Q. Wang, Z. Yu, A. Osman, Y. Yao, Y. Su, H. Yang and J. Lu, *ACS Nano*, 2024, **18**, 22648.
53 J. Wang, X. Cao, X. Cui, H. Wang, H. Zhang, K. Wang, X. Li, Z. Li and Y. Zhou, *Adv. Mater.*, 2024, **36**, 2311151.
54 H. Jiang, L. Ai, M. Chen and J. Jiang, *ACS Sustain. Chem. Eng.*, 2020, **8**, 10833.
55 Z. Lin, T. Wu, Y. F. Feng, J. Shi, B. Zhou, C. Zhu, Y. Wang, R. Liang and M. Mizuno, *ACS Appl. Mater. Interfaces*, 2022, **14**, 1034.
56 M. Shen, X. Zhao, L. Han, N. Jin, S. Liu, T. Jia, Z. Chen and X. Zhao, *Chem.–Eur. J.*, 2022, **28**, e202104137.
57 B. Jin, Y. Lu, X. Zhang, X. Zhang, D. Li, Q. Liu, B. Deng and H. Li, *Chem. Eng. J.*, 2023, **469**, 143906.
58 A. Ghaffar, M. Usman, M. U. Khan and M. Hassan, *J. Cleaner Prod.*, 2024, **446**, 141374.
59 Y. Cui, J. Liu, Z. Li, M. Ji, M. Zhao, M. Shen, X. Han, T. Jia, C. Li and Y. Wang, *Adv. Funct. Mater.*, 2021, **31**, 2106247.
60 X. Han, Z. Wang, M. Shen, J. Liu, Y. Lei, Z. Li, T. Jia and Y. Wang, *J. Mater. Chem. A*, 2021, **9**, 24452.
61 Y. Wang, J. Ju, W. Zhu, Y. Liu, Y. Zhang, W. Kang and B. Cheng, *J. Mater. Chem. A*, 2024, **12**, 24761.
62 R. Niu, J. Ren, J. J. Koh, L. Chen, J. Gong, J. Qu, X. Xu, J. Azadmanjiri and J. Min, *Adv. Energy Mater.*, 2023, **13**, 2302451.
63 L. Zhu, T. Ding, M. Gao, C. K. N. Peh and G. W. Ho, *Adv. Energy Mater.*, 2019, **9**, 1900250.
64 Y. Sun, Z. Zhao, G. Zhao, Y. Yang, X. Liu, L. Wang, D. Jia, X. Wang and J. Qiu, *J. Mater. Chem. A*, 2022, **10**, 9184.
65 Z. Wu, S. Chen, J. Li, B. Wang, M. Jin, Q. Liang, D. Zhang, Z. Han, L. Deng, X. Qu and H. Wang, *Adv. Funct. Mater.*, 2023, **33**, 2214327.
66 W. Wu, Y. Xu, X. Ma, Z. Tian, C. Zhang, J. Han, X. Han, S. He, G. Duan and Y. Li, *Adv. Funct. Mater.*, 2023, **33**, 2302351.
67 N. Li, L. Qiao, J. He, S. Wang, L. Yu, P. Murto, X. Li and X. Xu, *Adv. Funct. Mater.*, 2021, **31**, 2008681.
68 N. Li, K. Shao, J. He, S. Wang, S. Li, X. Wu, J. Li, C. Guo, L. Yu, P. Murto, J. Chen and X. Xu, *Small*, 2023, **19**, 2301474.
69 M. Saadi, A. Maguire, N. T. Pottackal, M. S. H. Thakur, M. M. Ikram, A. J. Hart, P. M. Ajayan and M. M. Rahman, *Adv. Mater.*, 2022, **34**, 2108855.
70 P. Zhu, Z. Yu, H. Sun, D. Zheng, Y. Zheng, Y. Qian, Y. Wei, J. Lee, S. Srebnik, W. Chen, G. Chen and F. Jiang, *Adv. Mater.*, 2023, **36**, 2306653.